JACS Au
AN OPEN ACCESS JOURNAL OF THE AMERICAN CHEMICAL SOCIETY

pubs.acs.org/jacsau

Article

Spatiotemporal Mapping of Local Heterogeneities during Electrochemical Carbon Dioxide Reduction

Hongyu An,[†] Jim de Ruiter,[†] Longfei Wu, Shuang Yang, Florian Meirer, Ward van der Stam,* and Bert M. Weckhuysen*

Cite This: *JACS Au* 2023, 3, 1890−1901

Read Online

ACCESS | Metrics & More | Article Recommendations | Supporting Information

ABSTRACT: The activity and selectivity of a copper electrocatalyst during the electrochemical CO_2 reduction reaction (eCO_2RR) are largely dominated by the interplay between local reaction environment, the catalyst surface, and the adsorbed intermediates. *In situ* characterization studies have revealed many aspects of this intimate relationship between surface reactivity and adsorbed species, but these investigations are often limited by the spatial and temporal resolution of the analytical technique of choice. Here, Raman spectroscopy with both space and time resolution was used to reveal the distribution of adsorbed species and potential reaction intermediates on a copper electrode during eCO_2RR. Principal component analysis (PCA) of the *in situ* Raman spectra revealed that a working electrocatalyst exhibits spatial heterogeneities in adsorbed species, and that the electrode surface can be divided into CO-dominant (mainly located at dendrite structures) and C−C dominant regions (mainly located at the roughened electrode surface). Our spectral evaluation further showed that in the CO-dominant regions, linear CO was observed (as characterized by a band at ∼2090 cm^{-1}), accompanied by the more classical Cu−CO bending and stretching vibrations located at ∼280 and ∼360 cm^{-1}, respectively. In contrast, in the C−C directing region, these three Raman bands are suppressed, while at the same time a band at ∼495 cm^{-1} and a broad Cu−CO band at ∼2050 cm^{-1} dominate the Raman spectra. Furthermore, PCA revealed that anodization creates more C−C dominant regions, and labeling experiments confirmed that the 495 cm^{-1} band originates from the presence of a Cu−C intermediate. These results indicate that a copper electrode at work is very dynamic, thereby clearly displaying spatiotemporal heterogeneities, and that *in situ* micro-spectroscopic techniques are crucial for understanding the eCO_2RR mechanism of working electrocatalyst materials.

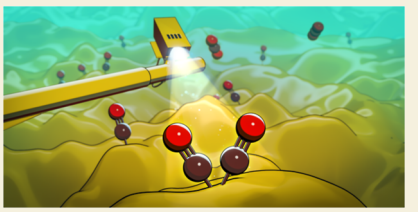

KEYWORDS: *CO_2 electroreduction, Raman spectroscopy, spatiotemporal spectroscopy, copper*

INTRODUCTION

The electrochemical carbon dioxide reduction reaction (eCO_2RR) to fuels and chemicals is a promising approach to store renewable energy in chemical bonds.[1−6] The activity and selectivity of electrocatalyst materials for eCO_2RR are largely dictated by the interplay between local environment (*e.g.*, electrolyte composition and pH) on one hand and the structure and composition of the catalyst material on the other hand.[7−12] For example, copper has the unique ability to form a variety of hydrocarbon products, and the selectivity toward ethylene and methane can be tuned by exposure of Cu(100) and Cu(111) surfaces, respectively.[13−22] While these characteristics make copper an interesting electrocatalyst material, directing the selectivity toward the production of a specific hydrocarbon product still remains challenging.[23−25] Oxide-derived Cu electrocatalysts quite often exhibit outstanding performance in eCO_2RR, especially in C−C coupling processes.[26−29] CO has been found to be a crucial intermediate in the eCO_2RR process on Cu, thus many research efforts have been devoted to elucidating the surface reactivity of CO and its relation with product formation.[14,30−33] Unfortunately, it remains challenging to reveal adsorbed intermediates beyond CO due to the dynamic nature of eCO_2RR. For example, the inevitable reduction of the oxidized electrode surface at cathodic bias and the accompanied surface reconstruction results in both temporal dynamic behavior and spatial heterogeneity of adsorbed surface species.[28,34,35]

The highly dynamic nature of the electrode surface under electrocatalytic operating conditions calls for a deeper understanding of the structure−performance relationships of copper-based electrocatalysts at work.[33,36−41] For this purpose, *in situ* and *operando* characterization techniques play an important role.[42] A lot of research has been conducted using analytical techniques with different spatial and temporal resolution, such as atomic force microscopy,[43] attenuated total reflection infrared spectroscopy (ATR−IR),[31,32,44] surface-enhanced Raman spectroscopy (SERS),[36,45−47] scanning electrochemical microscopy,[5,33] and synchrotron-based X-ray methods,[27,28] which provided valuable information about the

Received: March 22, 2023
Revised: June 11, 2023
Accepted: June 14, 2023
Published: July 6, 2023

https://doi.org/10.1021/jacsau.3c00129
JACS Au 2023, 3, 1890−1901

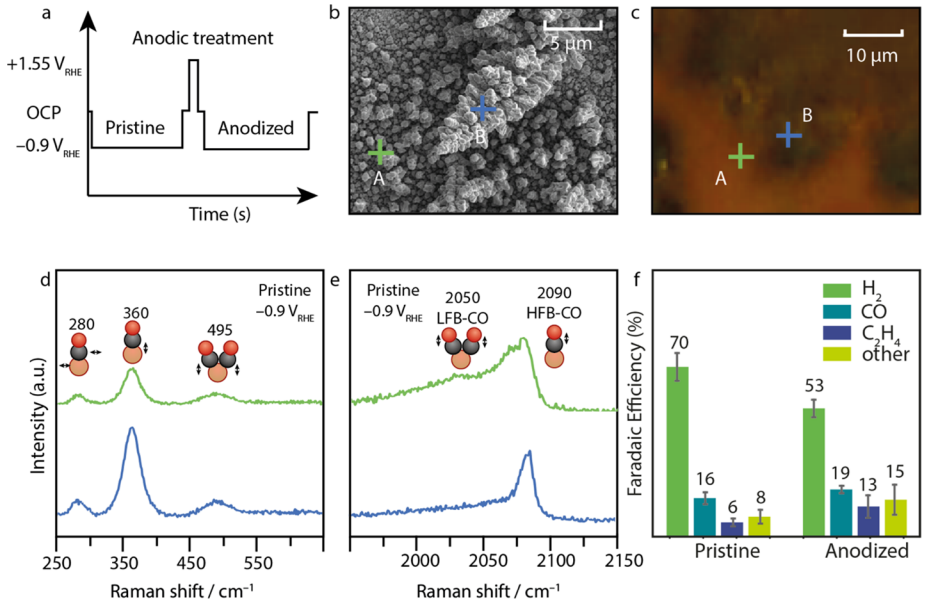

Figure 1. (a) Potential profile used in the work reported in this manuscript, indicating "pristine" and "anodized" eCO_2RR runs. (b) SEM and (c) optical microscopy image showing (after anodization) sites A and B, used for measuring the Raman spectra in panels (d,e). (d,e) *In situ* Raman spectra on site A (green) and site B (dark blue) at −0.9 V cathodic bias during pristine run in the low Raman shift region (d) and the CO stretch region (e), showing differences in the relative ratio of the LFB and HFB of surface bound CO, and the linear ν Cu−C vibration at ∼360 cm^{-1} and rotational δ Cu−CO vibration at ∼280 cm^{-1}. Another broad Raman feature at ∼495 cm^{-1} is observed as well at both points. (f) Faradaic efficiency (FE) for pristine and anodized electrodes, showing an increase in ethylene formation after anodization at the expense of hydrogen evolution. The error bars originate from averaging three different experiments.

details of the eCO_2RR and the restructuring of the copper surface under reaction conditions. However, many of the *in situ* and *operando* experiments still lack the combination of both temporal and spatial spectroscopic information to reveal reaction dynamics and heterogeneities on relevant space- and time-scales for the eCO_2RR. For example, static measurements are often insufficient to elucidate dynamic processes in a real catalytic process. Furthermore, spectroscopic information collected over a wide area gives averaged information, which is the case for ATR−IR spectroscopy and many synchrotron-based X-ray experiments, and therefore cannot reveal the spatial heterogeneity of a working electrocatalyst. However, more localized measurements, such as in many Raman micro-spectroscopy studies, need to be conducted with care, due to the potential risk of explaining the whole catalyst surface based on only few selected regions of a working catalyst that depend on the diffraction-limited spot size of the (visible) laser, which limits it to at best ∼0.5 μm.

Spatial variance in surface reactivity has already been suggested in many studies,[32] but not yet fully verified by spatiotemporal spectroscopic investigations. In this work, we utilize spatiotemporal Raman spectroscopy mapping to reveal heterogeneities of a copper electrode at work with micrometer resolution. With these *in situ* Raman micro-spectroscopy experiments, the spatial distribution and temporal evolution of surface intermediates was elucidated, and linked to the catalyst structure and performance by *ex situ* identical location electron microscopy and online product detection on the same time scale. Through spectral evaluation *via* principal component analysis (PCA) it was found that rough regions of the electrode, dominated by dendrites, are rich in intermediates that have previously been assigned to adsorbed CO at undercoordinated sites (*i.e.*, linear CO stretch at ∼2090 cm^{-1}, accompanied by linear Cu−C stretch at ∼360 cm^{-1} and Cu−CO rotational band at ∼280 cm^{-1}). More flat regions of the electrode are rich in intermediates that are ascribed to C−C coupling and ethylene formation (*i.e.*, low-frequency CO stretch at ∼2050 cm^{-1}), related to CO adsorbed on terrace sites. The dominant contribution of the C−C directing intermediate at different regions of the electrode surface is correlated to the appearance of a Raman feature at ∼495 cm^{-1}. The spatial distribution of these CO-dominant and C−C dominant regions was tuned by an anodic treatment, which roughens the surface and promotes the formation of active sites for C−C coupling in the subsequent reduction step. Through isotope labeling experiments, it became evident that this 495 cm^{-1} Raman feature is related to the presence of a Cu−C intermediate, which we infer to be another descriptor for hydrocarbon-based C−C directing reaction intermediates on reactive copper surfaces. When this 495 cm^{-1} Raman band is dominant, the classical 280, 360, and 2090 cm^{-1} Raman bands of linear adsorbed CO on copper are suppressed, and an increase in ethylene formation is observed. These results reveal the spatial heterogeneities of a working oxide-derived copper electrocatalyst surface and allow for a spectral footprint of surface reactivity.

RESULTS AND DISCUSSION

Spatial Heterogeneities of a Copper Electrode at First Glance

An electrodeposited Cu catalyst (abbreviated as Cu-EDP hereafter) was prepared based on reported methods,[34,35,48] and subjected to the potential profile shown in Figure 1a (current data in Figure S1). The potential profile roughened the electrode surface. A scanning electron microscopy (SEM) image of pristine Cu-EDP right after deposition is shown in Figures 1b and S2 and S3, in which tree-like dendrite structures on the length scale of several microns are visible.

https://doi.org/10.1021/jacsau.3c00129
JACS Au 2023, 3, 1890−1901

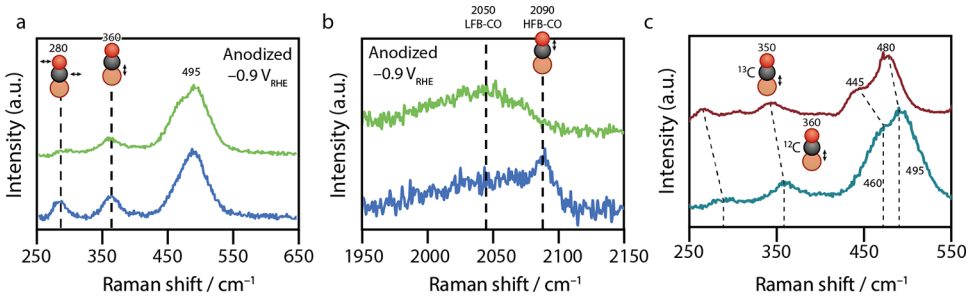

Figure 2. (a,b) *In situ* Raman spectra of site A (green) and B (dark blue) at −0.9 V cathodic bias during anodized run in (a) the low Raman shift region and (b) the CO stretch region, showing a dominant LFB of adsorbed CO in site A, accompanied by a dominant Raman feature at ∼495 cm^{-1}. (c) Raman spectra collected using $^{12}CO_2$ and ^{13}C-labelled CO_2. All potentials are *vs* RHE. Raman spectra collection time: 3 s for one pixel and 18 s for a complete Raman spectrum.

These dendrites are composed of nanoparticles with diameters around 20−50 nm. Next to the dendrites, more flat regions are also observed at the electrode surface, which also consist of individual Cu nanoparticles (see Figures S2 and S3). X-ray diffraction (XRD) data (Figure S4) show that the bulk of the sample consists of polycrystalline copper, while a clear XRD reflection of surface Cu_2O can also be discerned.[11] *In situ* Raman spectroscopy during the eCO_2RR was then conducted in a liquid phase flow cell (*i.e.*, 0.1 M CO_2-saturated $KHCO_3$ solution, pH = 6.8) in our previously reported setup and cell (Figure S5).[49] The Raman spectra at open circuit potential reveal that the surface of the electrode is dominated by Cu_xO_y (Figure S6), but these surface oxides are removed within a few seconds after cathodic bias onset. Due to the intrinsic roughened morphology, Raman signals can already be collected when pristine Cu-EDP is subjected to the eCO_2RR working conditions at −0.9 V due to the strong SERS effect (all potentials in this manuscript are *versus* reversible hydrogen electrode (RHE) and the data from this experiment are labelled as "pristine" throughout the manuscript). We have used 3 s exposure time for each spectral window, and the collection of one full Raman spectrum takes ∼18 s. These Raman spectra were collected 18 min after −0.9 V_{RHE} cathodic bias onset, at which the catalyst surface has stabilized, and observed spatiotemporal spectral variations that can be attributed to differences in adsorbed species. Segments of the Raman spectra of the pristine electrode collected at two representative points (*i.e.*, points A and B, indicated in the optical microscope image in Figure 1c (optical microscopy image of pristine electrode provided in Figure S2) in two spectral regions (low wavenumber region < 650 cm^{-1}, and CO region around 2000 cm^{-1}) are shown in Figure 1d,e to provide a quick view of spatial heterogeneity of a pristine copper electrode at −0.9 V_{RHE}. These two points in the microscopy image in Figure 1c correspond to the positions A and B in the SEM image in Figure 1b.

The main features that can be discerned at both points are the Cu−CO bending and Cu−C stretching vibrations in the low wavenumber region (*i.e.*, ∼280 and ∼360 cm^{-1}, respectively, Figure 1d) and the linear CO stretch vibrations on different adsorption sites between 2000 and 2100 cm^{-1} (Figure 1e). The 280 cm^{-1} Raman band is usually attributed to the restricted rotation of CO adsorbed on Cu, while the 360 cm^{-1} Raman band is assigned to the Cu−C linear stretching vibration.[30] The CO stretching vibrations in the 2000−2100 cm^{-1} region are usually deconvoluted into two bands: a relatively sharp Raman band at ∼2090 cm^{-1} is ascribed to CO adsorbed on isolated Cu sites [further referred to as "high frequency band (HFB) CO", or "HFB-CO" due to its higher Raman shift], and the broad Raman band in the region between 2020 and 2070 cm^{-1} is ascribed to CO adsorbed on terrace sites [further referred to as "low frequency band (LFB) CO" or "LFB-CO"].[14,18,30,31,36] Furthermore, bridged or multi-bound CO is typically observed <2000 cm^{-1} and often attributed to inactive spectator species, which are not observed in these spectra for the pristine electrode. Next to these different forms of CO stretching vibrations, a broad feature at ∼495 cm^{-1} is observed in the Raman spectra as well at both points A and B. Raman bands between 480 and 520 cm^{-1} have been discussed before in a few publications,[35,37,47] but the origin of these Raman bands and the related spectral assignments to adsorbed species are still a matter of debate and requires further attention. Some researchers attribute the 480−520 cm^{-1} Raman bands to Cu_x-OH_y species due to increased local alkalinity and severe hydrogen evolution or these bands are correlated with surface oxides (CuO_x),[30,50−52] or carbon-related species on a Cu surface.[35,37] One of the goals of this study is to further elucidate the origin of this Raman feature. Hence, our *in situ* spatiotemporal Raman spectroscopy mapping study aims to correlate the temporal appearance of the 480−520 cm^{-1} Raman band to other spectral features, and link it to the dominant surface morphology through a quasi-identical location *ex situ* SEM experiment. In this way, Raman spectra can become a direct measure for the surface morphology and Cu electrode performance. While all the CO-related features discussed above are present on all points to different extents, the exact shape of the *in situ* Raman spectra are quite different across the surface of the Cu electrode. The Raman spectra collected at points A and B already show spectral variations, suggesting the complex nature of electrocatalysts (especially oxide-derived Cu), which calls for improved spatiotemporal investigations and detailed analysis of the spectral footprint of a copper electrode under operational conditions.

Surface Roughening through Anodic Treatment

Anodic treatment has been reported to be effective for boosting the formation of ethylene.[49,53−55] To further investigate the underlying eCO_2RR mechanism on pristine and oxide-derived copper electrodes, an anodization step was applied (+1.55 V for 120 s) before the second eCO_2RR reduction step (corresponding experiments denoted as "anodized" in the rest of the manuscript). As expected, the strong anodization of the surface enhanced C−C coupling and resulted in a 2-fold increased ethylene production at the

https://doi.org/10.1021/jacsau.3c00129
JACS Au 2023, 3, 1890−1901

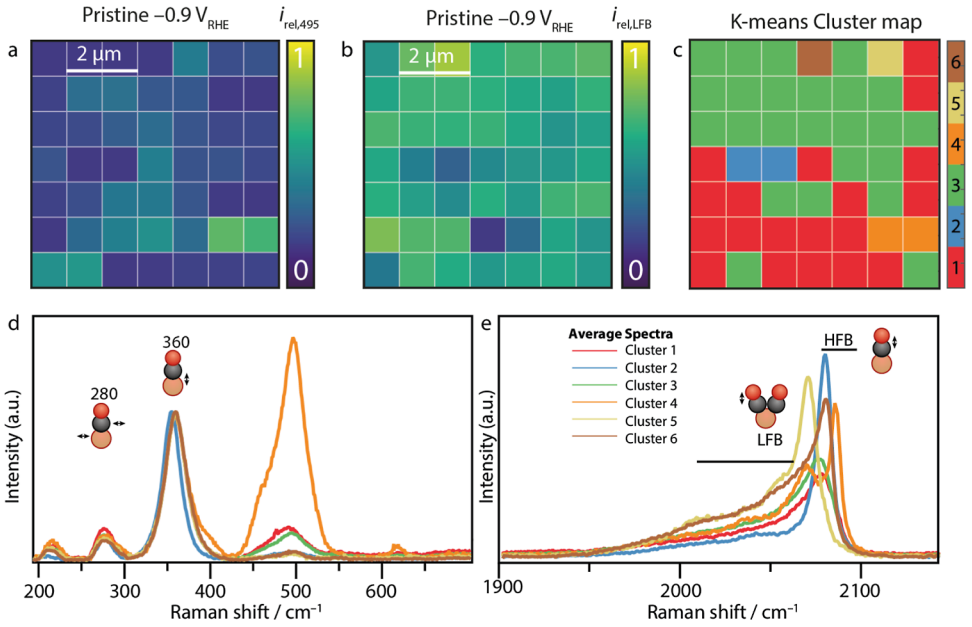

Figure 3. (a) Raman heatmap in the low Raman shift region and (b) CO stretching region, showing the spatial distribution of relative intensities of the 495 cm^{-1} Raman peak ($i_{rel,495}$) and LFB of CO at 2000−2070 cm^{-1} ($i_{rel,LFB}$) during the pristine run. (c) Result of PCA & *k*-means clustering performed with the single pixel spectra of the spatially resolved micro-Raman data. *k*-means clustering using six clusters in 3-dimensional PC space resulted in the displayed segmentation of the map. (d) Average spectra of the segmented regions (clusters) shown in (c) zooming in on the low Raman shift region and the CO stretch region (e), respectively. Figure S13 contains the spectra over the entire range.

expense of hydrogen evolution (Figure 1f). The same anodization treatment was performed on points A and B from Figure 1 during the Raman micro-spectroscopy measurements. The cathodic potential after this anodization was set at −0.9 V and the corresponding Raman signals in the low Raman shift region and CO stretch region are shown in Figure 2a,b. Significant changes in the Raman signals are observed after the anodization compared to the pristine electrode (Figures 1d,e, S7, and S8). First of all, the Raman band centered at ∼495 cm^{-1} has become the dominant feature in the low Raman shift region at both points at the expense of the Raman bands centered at ∼280 and ∼360 cm^{-1}. The CO stretch vibrations at ∼2050 and ∼2090 cm^{-1} also undergo changes upon anodization (Figure 2b), which is reflected by the fact that the relative intensity of the HFB-CO Raman band decreases on both sites A and B, and that the LFB-CO Raman band rises in relative intensity and becomes the dominant feature for site A, where little to no contribution from HFB-CO could be discerned (Figure 2b). The dominant LFB Raman band is clearly accompanied by a more dominant 495 cm^{-1} Raman band, suggesting that they might be correlated. Interestingly, in site B, there is still a significant contribution from the HFB-CO species, accompanied by more pronounced Raman features at ∼280 and ∼360 cm^{-1}.[36]

To elucidate the origin of these low Raman shift region features, we have collected the Raman spectra using isotope labelled $H^{13}CO_3$ and $^{13}CO_2$ (Figure 2c). An isotopic shift of −15 cm^{-1} is clearly visible (from 495 to 480 cm^{-1}) when ^{13}C-labelled CO_2 is used, which is very close to the theoretical value of −18 cm^{-1} for a Cu−C stretching vibration using the harmonic oscillator model.[37] We note that the features at ∼500 cm^{-1} consist of at least two Raman bands (Figure 2c), which shift by a different amount upon isotope labelling, suggesting they originate from distinct surface adsorbates. Considering the increase in ethylene production and the relative increase of the Raman bands at ∼500 cm^{-1} after the anodization, it is suggested that these bands could be due to the presence of ethylene-directing surface adsorbates. Therefore, we tentatively ascribe these Raman features to Cu−C surface adsorbates at the Cu surface that are (mainly) involved in C−C coupling. Finally, by correlating these *in situ* Raman data to the *ex situ* SEM analysis before and after eCO2RR, we can conclude that the dendrite regions of the electrode surface are prone to give rise to stable linear CO species located at undercoordinated sites, whereas the flatter parts of the Cu electrode give rise to the formation of C−C directing surface adsorbates at planar Cu facets.

Spatiotemporal Correlation of the Raman Features for the Pristine Electrode through PCA

To provide insights on the spatiotemporal distribution of the surface adsorbates observed, *in situ* Raman micro-spectroscopy mapping experiments were performed (Figure 3). We have collected the Raman signal from a 7 μm by 7 μm field of view using an interval and diffraction-limited spot size of ∼1 μm (1.2 μm according to Airy disk diameter, NA = 0.8), resulting in 49 Raman spectra in total. The Raman micro-spectroscopy maps are constructed in a raster scan fashion, from top left to bottom right. All Raman spectra for the pristine electrode at −0.9 V_{RHE} can be found in Figure S7, and for the anodized electrode over the same area in Figure S8. We note that some spectral and sample drifts and surface restructuring of the sample is possible under the electrochemical conditions applied, which would influence the spatiotemporal spectral features discussed below. To check for possible sample drifts as well as surface restructuring, two consecutive Raman maps were collected (Figure S9). This experiment shows that the CO-dominant regions and regions where C−C directing Cu−C intermediates dominate roughly remain at the same spatial positions, thereby confirming that drift and catalyst restructuring has minimal influence. To visualize the spatial hetero-

https://doi.org/10.1021/jacsau.3c00129
JACS Au 2023, 3, 1890−1901

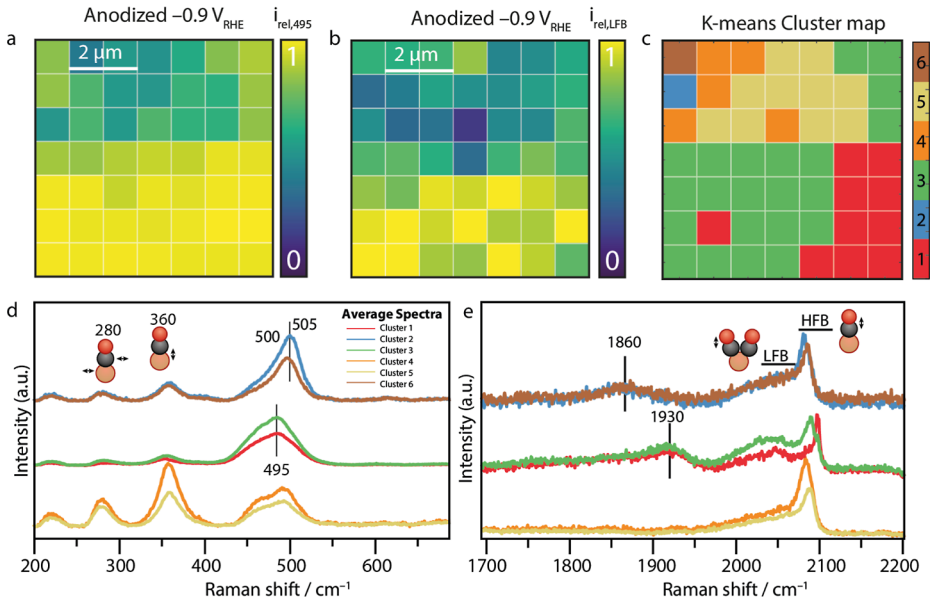

Figure 4. (a) Raman heatmap in the low Raman shift region and (b) CO stretching region, showing the spatial distribution of relative intensities of the 495 cm^{-1} Raman peak ($i_{rel,495}$) and LFB CO at 2000–2070 cm^{-1} ($i_{rel,LFB}$) during the anodized run. (c) Result of PCA and *k*-means clustering performed with the single pixel spectra of the spatially resolved micro-Raman mapping data. *k*-means clustering using 6 clusters in 3-dimensional PC space resulted in the displayed segmentation of the map. (d) Average spectra sorted by the cluster results in (c) of the low Raman shift region and (e) CO stretch region, respectively. Figure S13 contains the spectra over the entire range.

geneities of the active Cu electrode surface and derive correlations between vibrational features in low Raman shifts and the CO region, heatmaps of the spectra are plotted (Figure 3). In these heatmaps, the ratio between the dominant feature and the minor species was calculated accordingly: in the low Raman shift region, the intensity of the Raman band at ~495 cm^{-1} is divided by the sum of all surface adsorbate species in the spectral region 300–540 cm^{-1} ($i_{rel,495}$), (Experimental Section). In the CO stretch Raman region (~2000 cm^{-1}), the intensity of the 2000–2075 cm^{-1} LFB-CO band is compared to the sum of all surface adsorbate species in the spectral region 2000–2100 cm^{-1} ($i_{rel,LFB}$). By using these ratios, we also exclude variations in the SERS effect at different locations at the Cu electrode surface as a possible explanation for changes in the spectral features. The relative peak intensities are calculated based on fitting of the Raman spectra. Examples of relevant spectral fits are given in Figure S10. It should be noted that the spectral features vary quite a lot across the measured area, given the complex surface condition of the spots. This data processing presents the overall trends in ratios, rather than quantitative details. For the same reason, species of similar nature are quantified into one group, although it should be evident that the exact shape of the HFB and LFB features can be quite different at different sites, and the 495 cm^{-1} Raman band can be discerned as a doublet peak at certain sites, as discussed above. The Raman heatmap confirms that the Raman bands located ~280 and ~360 cm^{-1} as well as the Raman band assigned to HFB-CO surface adsorbate species are dominating for the pristine catalyst at −0.9 V$_{RHE}$ (Figure 3a,b). The relative intensity of the Raman band at ~495 cm^{-1} compared to the total intensity of spectral features in the low Raman shift region is almost zero (Figure 3a), and the LFB/(LFB + HFB) ratio is ~0.5 over the entire Cu surface (Figure 3b).

Next, PCA and *k*-means clustering of the 49 spectra was performed to identify spectral similarities in an unbiased manner. Based on the scree plot and inspection of the eigenspectra, the first three principal components (PCs) were selected, capturing 95% of the data's variance (Figure S11). The resulting 3-dimensional score plot was then segmented into 6 clusters using *k*-means clustering, effectively pooling spectra based on their spectral similarity, which is expressed by their proximity in the score plot. The number of clusters was chosen based on the inspection of the averaged spectra of each cluster and 6 clusters provided a sufficiently fine-grained model to capture even single-pixel regions with a spectroscopically distinct fingerprint. Figure 3c shows the distribution of the 6 spectroscopically distinct areas (the clusters) and the spectral regions of interest of the corresponding average spectra of the low Raman shifts and CO stretch region in panels, Figure 3d,e. Note that the segmentation of this map into 6 clusters is exclusively based on spectral similarity and not on any spatial correlation.

The cluster map shows that most of the Raman data is described by two clusters (cluster 1 and 3, red and green, respectively), and only 6 out of the 49 Raman spectra differ significantly from the average spectra of these clusters, showing the homogeneous nature of the pristine Cu electrode. The averaged Raman spectra in Figure 3d,e were normalized on the 360 cm^{-1} peak to clearly visualize the intensity ratio difference, similar to the ratios presented in Figure 3a,b. Upon closer inspection of the average spectra of clusters 1 (red) and 3 (green), it can be seen that their separation is mainly based on their slight peak shift in the 495 cm^{-1} region and the difference in ratio of the 280 and 360 cm^{-1} Raman bands (Figure S12). In cluster 3, the spectra have a relatively higher 360/280 cm^{-1} band intensity ratio compared to the spectra in cluster 1. Moreover, the relative intensity of the LFB is higher for cluster 3 compared to cluster 1. From recent literature, it is known that an increased 360/280 cm^{-1} band intensity ratio is correlated to a higher *CO coverage and increased formation of ethylene.[26] The 360/280 cm^{-1} band intensity ratio of the 6

https://doi.org/10.1021/jacsau.3c00129
JACS Au 2023, 3, 1890–1901

clusters is shown in Figure S12. Furthermore, our previous work showed that ethylene formation is boosted when low frequency CO surface adsorbates were present. Both observations are present in cluster 3, which shows the strength of the PCA and *k*-means clustering approach applied to our micro-spectroscopic Raman data. A main observation is the variation in the maxima of the HFB CO between the different clusters. The vibrational energy of the CO band is dependent on the surface Cu facets or sites on which the CO is adsorbed. The characteristic sharp feature of the HFB CO varies between 2070 and 2090 cm^{-1} and therefore acts as a local surface probe for the heterogeneous nature of the electrode surface. A very intense spectral feature at 500 cm^{-1} isolates the two pixels that constitute cluster 4 (orange label) from the other clusters. This is also evident in the Raman heatmap, shown in Figure 3a.

What could have been missed without the use of clustering, are the three other isolated clusters: clusters 2, 5, and 6 (blue, yellow, and brown). These clusters are mainly separated based on the position of the sharp HFB CO peak. The shift of this peak indicates the presence of morphological heterogeneities (exposed facets/defects sites) over the measured area with different adsorption energies for Cu−CO. For cluster 2, the position of the Cu−C stretch vibration (355 cm^{-1}) of the Cu−CO is significantly lower in energy while having the highest CO stretching (2090 cm^{-1}) vibrational energy of all the clusters, suggesting a strong CO bond and weaker Cu−C bond, hence, probing an active site that most probably produces CO (g) as products. The mapping data combined with the *k*-means clustering analysis shows that intermediates (in this case, mainly CO intermediates with different binding strengths) on various active sites can be discerned on polycrystalline copper surfaces.

Spatiotemporal Correlation of the Raman Features of the Anodized Electrode through PCA

After an anodization step, the proportion of the surface adsorbate species associated with the Raman bands located at ∼495 cm^{-1} as well as the proportion of the LFB-CO surface adsorbate species significantly increased during the subsequent eCO_2RR run at −0.9 V *vs* RHE (Figure 4a,b). More specifically, the bottom half of the imaged area is dominated by the Raman bands at ∼495 cm^{-1}, and the relative Raman intensity of the LFB-CO surface adsorbate also increases and dominates accordingly in the same area. These Raman heatmap images indicate that Cu surface sites have been created during anodization on which different surface adsorbates can be observed that potentially serve as a spectral fingerprint of local variations in catalytic performance.[46] Furthermore, the dominant presence of the Raman band at ∼495 cm^{-1} coinciding spatially with Raman bands assigned to LFB-CO surface adsorbates suggests they are indeed correlated, as was already inferred above by comparison of the spectra at point A and B shown in Figure 2. Collection of the full Raman maps (each consisting of 49 spectra) typically takes 18 min in total. Again, to exclude the possibility that the signal associated with different surface adsorbates changes throughout the acquisition of the Raman maps due to surface restructuring or sample drift, we performed repeated spatial-resolved SERS experiments and confirmed that the observed spatiotemporal variations are not caused by the time-resolved dynamic behavior of the surface or *e.g.*, the direction of scanning (Figure S9).

With the same PCA & *k*-means clustering analysis as applied on the pristine sample (differences visualized in Figure S13), again four distinct clusters can explain the data in the map together with two single point clusters, *i.e.*, blue and brown, Figure 4c (PCA and scree plots in Figure S14). The average spectra for each cluster were calculated and displayed in Figure 4d,e. For clarity, we have separated the average Raman spectra in three parts based on similarities in spectral features. All six average spectra show features in the 500 cm^{-1} region, but vary in intensity of the Cu−CO bands at 280 and 360 cm^{-1}. In the top of the Raman map, the surface contains more Cu−CO compared to the bottom, as indicated by the Raman spectra of cluster 4 and 5. This is also accompanied by a more pronounced presence of the HFB CO Raman band. The bottom part contains more Raman features in the 500 cm^{-1} region and subsequently more LFB CO, which shows that the combined (unsupervised) PCA and *k*-means clustering shows a similar correlation as was indicated by the heatmaps of Figure 4a,b, namely a CO-dominant region and a region in which intermediates around 500 cm^{-1} dominate, which are inferred to be related to Cu−C intermediates involving C−C coupling.

Compared to the pristine sample, new features are observed in the averaged anodized spectra at 1930 cm^{-1} (*i.e.*, cluster 1 and 3, red and green) and 1860 cm^{-1} (*i.e.*, cluster 2 and 6, blue and brown). Signals at these Raman shifts are ascribed in the literature to Cu−CO species with a reduced CO bond strength, such as multi-bound Cu−CO or bridged CO.[36] Furthermore, the peak position in the low Raman shift spectral window for clusters 1 and 3 is slightly lower (495 cm^{-1}) than that of clusters 2 and 6 (500/505 cm^{-1}). This trend is reversed for the two CO features; clusters 1 and 3 contain a 1930 cm^{-1} feature and clusters 2 and 6 a Raman band at ∼1860 cm^{-1}. Considering the presence of CO surface adsorbate species, a lower vibrational energy of the CO stretch bond suggests that the electron density is located more at the Cu−C bond, hence, thereby increasing the Cu−C bond stretching energy. Using this concept, the Raman bands located at ∼500 cm^{-1} could be correlated to the lower CO vibrations. Considering the general increase in the formation of ethylene after anodization of the Cu electrode, these Raman bands could be originating from ethylene directing surface adsorbate species. Fundamentally, any reduction reaction (*e.g.*, hydrogenation and CO−CO coupling) with adsorbed CO would result in a reduction of the CO bond strength due to the change in hybridization of the carbon atom. With the simple use of both concepts, we tentatively ascribe the Raman bands located at ∼500 cm^{-1} to ethylene directing surface adsorbate species that are in a more reduced stage than surface adsorbed CO species. Considering clusters 4 and 5, we cannot assign the bands at ∼500 cm^{-1} to be originating from the same species as the bands observed at 1860 and 1930 cm^{-1}. In these clusters, bands at ∼460 and ∼495 cm^{-1} are present, but signals lower than 1950 cm^{-1} are very low or absent. However, as also seen in the heatmaps of Figure 4a,b, the LFB-CO signals remain present following the correlation of LFB-CO and the 495 cm^{-1} region, as described before. The LFB-CO is typically ascribed to CO adsorbed on Cu terrace sites (such as Cu(100) surfaces), and in our previous work, we showed that these are a crucial condition for the necessary CO−CO coupling for C_2 product formation, whereas HFB-CO is related to adsorbed CO on corners and edges. The fact that both the LFB-CO and 495 cm^{-1} Raman bands also increased in relative intensity after anodization of the Cu electrode highly suggests that these Raman bands are

https://doi.org/10.1021/jacsau.3c00129
JACS Au 2023, 3, 1890−1901

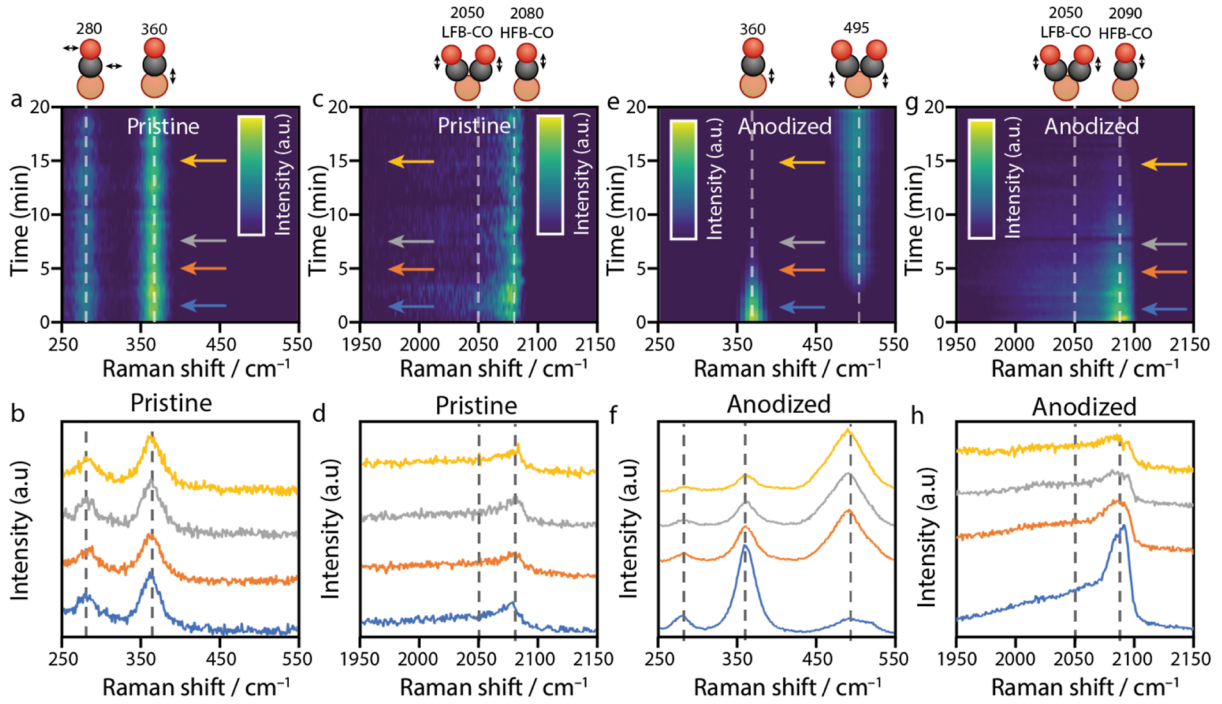

Figure 5. (a, c, e, g) Temporal *in situ* Raman micro-spectroscopy heatmaps and (b, d, f, h) selected Raman spectra for the pristine Cu electrode (a–d) and the anodized Cu electrode (e–h). Colored arrows in (a, c, e, g) correspond to the spectra in (b, d, f, h). (a) Temporal *in situ* Raman micro-spectroscopy heatmap in the low Raman shift region, and (b) the corresponding spectra at selected time intervals for the pristine Cu electrode. (c) Temporal Raman micro-spectroscopy heatmap in the CO stretch region, and (d) the corresponding spectra at selected time intervals for the pristine Cu electrode. (e) Temporal *in situ* Raman micro-spectroscopy heatmap in the low Raman shift region, and (f) the corresponding Raman spectra at selected time intervals for the anodized Cu electrode. (g) Temporal *in situ* Raman micro-spectroscopy heatmap in the CO region, and (h) the corresponding spectra at selected time intervals for the anodized electrode. Potential: −0.9 V *vs* RHE. Collection time: 3 s per scan and 18 s for a whole Raman spectrum.

correlated and linked to C−C directing surface adsorbate species. Finally, when the spatiotemporal *in situ* Raman micro-spectroscopy maps are combined with the *ex situ* SEM images, it can be concluded that dendrites at the Cu electrode surface are prone to CO formation, whereas Cu nanoparticles on more planar areas of the electrode favor deeper CO reduction and seems to be related to ethylene formation. All discussed vibrations in this work, and our previous work, are summarized in Table S1.

Correlation between 495 cm^{-1} Raman Feature and Ethylene Formation

Elucidation of a potential intermediate surface species and linking them to a plausible reaction mechanism is a crucial topic of research in the field of catalysis, which also applies to the eCO_2RR process. To correlate the spatiotemporal surface adsorbate species as observed with *in situ* Raman micro-spectroscopy with catalytic performance, we have performed eCO_2RR activity measurements and analyzed the time-dependent FE of ethylene and CO using gas chromatography (GC) on a similar timescale as the Raman micro-spectroscopy measurements. From this analysis, it becomes evident that the FE of ethylene experienced a 2-fold increase during the anodized eCO_2RR run. The notion that anodization of the Cu electrode creates ethylene-forming surface adsorbate sites (Figure 1f) is further strengthened by our temporal Raman micro-spectroscopy experiments, which are displayed in Figure 5. The arrows in the heatmaps denote the position of the plotted spectra in the bottom of Figure 5. The Raman spectra of the pristine sample remain almost constant over time during the eCO_2RR run (Figure 5a,c, 20 min total run time), with the Raman bands at ∼280 and ∼360 cm^{-1} as dominant spectral features that persist throughout the experiment. This can be more clearly observed from the Raman spectra at selected time intervals (Figure 5b,d). It is worth noting that in this specific location, the Raman band at 495 cm^{-1} was not observed, unlike in Figure 1d. However, we consider this to be a consequence of the spatial heterogeneity of the electrode surface, further emphasizing the importance of Raman mapping as a tool to characterize surface species of a working electrocatalyst.

The temporal trend is very different for the anodized Cu electrode. For the anodized sample, the surface adsorbate species associated with the 280 and 360 cm^{-1} Raman bands are still dominating in the first 4 min after cathodic bias onset, after which the 495 cm^{-1} Raman band increases in intensity, while the 280 and 360 cm^{-1} Raman bands fade away at the same point in time (Figure 5e,f). After 7−8 min, the Raman band located at ∼495 cm^{-1} is largely dominating the spectra, while the 280 and 360 cm^{-1} Raman bands become very weak. Meanwhile, the total intensity of the HFB and LFB bands associated with surface adsorbed CO species decreases, although the HFB CO band is clearly affected more over time (Figure 5g,h). Since the intensity of the 495 cm^{-1} Raman band remains almost constant, it is plausible to attribute the decrease of HFB-CO signal to less CO adsorbed at the Cu electrode, rather than a decrease of the overall SERS effect. The decrease in SERS intensity of adsorbed CO signal during ethylene-producing conditions has also been observed in our previous report[35] as well as recent publications.[18,56] The LFB band of surface CO decreases in intensity at a slower rate,

https://doi.org/10.1021/jacsau.3c00129
JACS Au 2023, 3, 1890−1901

leading to a higher relative intensity of the LFB of surface CO at longer reaction time compared to the HFB of surface CO (time profile of $i_{rel,LFB}$ can be found in Figure S15). The GC time profile (Figure S16) indicates that the sample exhibits an increased ethylene selectivity over time, with peak FE (17%) towards ethylene in the 20 min time window. Although the time for a GC measurement is relatively slow compared to a Raman spectroscopy measurement, it is evident that the sample possesses a relatively high FE towards ethylene when the surface is dominated by the Raman band at ∼495 cm^{-1} and LFB-CO centered at ∼2050 cm^{-1}, which are proposed to correspond to the Cu−C and linear CO stretch vibrations of a C−C directing intermediate, respectively. This suggests that the transition toward an activated Cu surface, which is dominated by 495 cm^{-1} Raman features, is correlated with the activation of the anodized Cu-EDP sample toward ethylene production, and the Cu surface transforms from CO-dominating to C−C-dominating upon anodic treatment. Based on our findings, we tentatively assign the Raman bands located at ∼495 cm^{-1} to a surface adsorbate species that constitutes and important step in the eCO_2RR mechanism beyond *CO.

The higher Raman shift of the 495 cm^{-1} Cu−C Raman band compared to that of the linear Cu−C vibration at 360 cm^{-1} suggests that the corresponding surface adsorbate has a stronger Cu−C bonding than a linear Cu−CO. This is in line with a C−C directing intermediate and the lower Raman shift of LFB-CO compared to HFB-CO, which suggests that more electron density is on the Cu−C bond and less on the CO bonds. Evolution of its intensity over time also suggests that the 495 cm^{-1} Raman feature likely originates from the linear Cu−CO species. In other words, we argue that the 495 cm^{-1} Raman feature grows at the expense of the 360 cm^{-1} Raman feature (Figure 5e). Its increased intensity is also accompanied by increasing relative intensity of LFB-CO, which has been inferred to favor CO−CO coupling. These phenomena taken together make it plausible to assign the Raman band at ∼495 cm^{-1} to a deeper reduction surface intermediate than Cu−CO which is related to ethylene formation. Potential candidates for such deeper reduction surface intermediate are CO−CO and CO−COH, which are very difficult to distinguish spectroscopically.[57−59] It should be noted that although Cu-EDP is very useful in spectroscopic studies (due to the strong SERS effect and minimized influence of bubbles at low conversion), the general production of ethylene is low compared to other Cu-based catalyst. However, the observed trend that the relative intensity of the 495 cm^{-1} feature increases upon going from pristine to anodized copper surfaces, suggests that the 495 cm^{-1} bands play a key role in ethylene production. It is also worth noticing that further anodization−reduction cycles do not lead to an increased FE towards ethylene. Our *in situ* Raman spectroscopy measurements indicate (Figure S17) that after two anodization cycles, a wide Raman band centered at ∼1930 cm^{-1} becomes apparent, which is well separated from the rest of the CO species in the 2000−2100 cm^{-1} region. This Raman band was not observed for the pristine sample (Figure 3) and only contributed to the spectral footprint in a minority of the Cu electrode surface for the anodized sample (Figure 4) at the same cathodic bias. This very low vibrational frequency is in line with the bridged or multi-bound CO species reported in the literature,[60] which is usually considered to be inert or a spectator species in eCO_2RR.[31,61] This also implies that CO peaks below the 2000 cm^{-1} line should be assigned to bridged or multi-bound CO. We find that this bridged/multi-bound CO band is accompanied by an intense Raman band at ∼480 cm^{-1}, suggesting they are correlated, as was also inferred by the *k*-means clustering analysis in Figure 4. This is in line with the expected vibrational energy shift for the Cu−C vibration of bridged/multi-bound CO compared to linear CO, since more electron density is on the Cu−C vibration in bridged-CO, resulting in a stronger bond and higher Raman shift. This also means that the assignment of the Raman band located at ∼495 cm^{-1} to the Cu−C vibration of a C−C directing intermediate is reasonable, as we explained above: the electron density is largely on the Cu−C bond, which in turn also weakens the CO bond strength and results in a shift from HFB-CO to LFB-CO. Furthermore, the Raman peak position implies that the Cu−C bond of the C−C directing intermediate is stronger than bridged-CO, which favors hydrogenation of the CO moieties, resulting in C_{2+} hydrocarbons, such as ethylene.

Based on the spatiotemporal *in situ* Raman spectroscopy data described above, we are now in a position to discuss the reaction mechanism for the eCO_2RR process on pristine and oxide-derived Cu-EDP during the anodization−reduction cycle. We propose that CO_2 is reduced at a relatively fast rate on pristine Cu-EDP into Cu−CO adsorbed on under-coordinated sites at the surface. This surface adsorbate species is characterized by Raman features at ∼280 and ∼360 cm^{-1}, as well as a strong HFB-CO peak at ∼2090 cm^{-1}, in line with previous observations.[34,35,47,50] Further reduction of this Cu−CO is inhibited and thus becomes the rate determining step towards ethylene formation (6% FE), resulting in *CO desorption and dominant gaseous CO formation (11% FE). After anodization of the Cu electrode, more active sites for ethylene formation are created after the subsequent reduction (hence the observed 2-fold increase in FE), while the CO production remained constant. In literature, these ethylene formation sites are typically ascribed to Cu terrace sites (*e.g.*, Cu(100) surfaces) or the junction of different facets (*e.g.*, Cu(110) edges in Cu cubes), which facilitates C−C coupling due to the close proximity of multiple CO molecules.[18,62] These surface sites exhibit faster kinetics for the further conversion of Cu−CO into a more deeply reduced intermediate, because the CO intermediate is optimally bound to the surface and does not desorb before further hydrogenation occurs. However, if multiple anodization cycles are performed, the binding strength of CO at the surface becomes too large, resulting in the appearance of bridged/multi-bound CO, which is considered to be an inactive spectator species in eCO_2RR. The improved kinetics after one anodization−reduction cycle causes a further step than the reduction of Cu−CO to become the new rate-limiting step. In this case, a newly formed surface adsorbate species beyond Cu−CO, characterized by a stronger Cu−C bonding (as evidenced by a spectral shift of the Raman band for the Cu−C species at ∼495 cm^{-1} during ethylene formation as compared to the Raman band for the Cu−C species at ∼360 cm^{-1} during CO formation), becomes a plausible reaction intermediate before the kinetic bottleneck and thus dominates the surface during the *in situ* Raman micro-spectroscopy measurements. This is reflected in the higher intensity of the 495 cm^{-1} Raman feature and the lower intensity of the 280 and 360 cm^{-1} Raman features, as well as the improved FE towards ethylene. Our spatiotemporal spectroscopic investigations hence provide a spectral footprint for catalytic activity of a copper electrode

https://doi.org/10.1021/jacsau.3c00129
JACS Au 2023, 3, 1890−1901

surface: when the Raman feature at ∼360 cm^{-1} dominates the spectra, more CO is produced, whereas when the Raman feature at ∼495 cm^{-1} dominates the spectra, more ethylene is produced. Furthermore, the involvement of the Cu−C surface species characterized by the 480 cm^{-1} Raman band, implies the dominant presence of spectator species, namely bridged/multi-bound CO. These spatial Raman micro-spectroscopy maps revealed the heterogeneity of an anodized copper electrode under cathodic bias, which can be split into two main regions as described above: CO forming and C−C products forming.

CONCLUSIONS

Spatiotemporal *in situ* Raman spectroscopy mapping has been used to elucidate the local heterogeneities and mechanism of the eCO_2RR on an oxide-derived Cu electrocatalyst material before and after applying an anodization treatment. The measurements reveal that a real electrocatalyst displays heterogeneities in the surface adsorbates during reaction, which remain often unnoticed when an ensemble analytical measurement is used. More specifically, domains with CO or C−C directing surface adsorbates were observed, and a boost in C−C directing sites is observed after an anodization−reduction cycle. These different reaction intermediates resulted in different activities and selectivities, as evidenced by online product analysis. Due to the correlation between the LFB of CO (LFB-CO), located at ∼2050 cm^{-1}, and a dominating feature at ∼495 cm^{-1} after anodization, we attribute this spectroscopic feature to the presence of an ethylene-forming reaction intermediate based on PCA combined with *k*-means clustering of the spatial Raman micro-spectroscopy maps. This finding corroborates the 2-fold increase in FE for ethylene observed with online product analysis on the same time scale, whereas the other C-containing reaction products are unaffected by the anodization cycle. This observation is further supported by ^{13}C-labelling experiments, which showed that the correlated spectroscopic features at ∼495 and ∼2050 cm^{-1} are indeed best explained by the presence of a Cu−CO surface adsorbate species. An updated table of vibrational peak assignments of our previous work and this work is provided in the Supporting Information (Table S1). Temporal *in situ* Raman spectroscopy measurements reveal that the active sites formed after the anodization process and characterized by the Cu−C feature with a Raman band at ∼495 cm^{-1} become dominant after ∼10 min of eCO_2RR onset at the expense of the Cu−CO feature, which is observed at ∼360 cm^{-1}. This time-dependent observation suggests that the 495 cm^{-1} Raman band is most probably connected to a deeper reaction intermediate than Cu−CO, with a stronger Cu−C bond, which facilitates further hydrogenation toward C_2 hydrocarbon products, such as ethylene. Furthermore, the presence of the Raman bands at ∼460 and ∼1950 cm^{-1} is indicative of bridged/multi-bound CO. This shows that the low Raman shift region allows to determine a range of surface adsorbates, of which some can be regarded as C−C directing reaction intermediates, and hence can be used as spectroscopic evidence for catalyst performance. Hence, these results stress the importance of studying the spatial heterogeneities as well as the time evolution of a working electrocatalyst to elucidate a catalytic reaction mechanism, thereby providing further insights to the evolution of reaction pathways toward *e.g.*, C_2 products (*i.e.*, ethylene) on oxide-derived Cu electrocatalysts during eCO_2RR.

EXPERIMENTAL SECTION

Chemicals

Copper foil (Cu, purity: 99.9999%, Puratronic) was purchased from Alfa Aesar. Potassium bicarbonate ($KHCO_3$, purity > 99.7%) was purchased from Fluka. Sulfuric acid (H_2SO_4, AnalaR NORMAPUR analytical reagent, 95−97%) was purchased from VWR Chemicals. Carbon dioxide gas (CO_2, purity: 99.995%) was purchased from Linde Gas. Polishing powders (5 μm CeO_2 and 1 μm Al_2O_3) were purchased from Bodemschat. copper(II) sulfate pentahydrate ($CuSO_4{\cdot}5H_2O$, purity >99%) was purchased for Sigma-Aldrich.

Sample Preparation

For the preparation of the Cu-EDP sample, the Cu foil was cut into strips, then polished with 5 μm CeO_2 and 1 μm Al_2O_3 polishing powders. Then the sample was sonicated in deionized water (Milli-Q) for 2 min, immersed in 1 M HNO_3 for 1 min, then sonicated in Milli-Q water for 5 min, and rinsed with flowing deionized water for 5 min. The sample was then immersed into a solution containing 1 M H_2SO_4 and 0.2 M $CuSO_4$. The electrodeposition was conducted under chronopotentiometry program (constant current density). Current density was set at −100 mA/cm^2. Another piece of polished Cu foil was used as counter electrode.

Sample Characterization

XRD measurements were performed on a Bruker D2 PHASER diffractometer using Co Kα (1.789 Å) radiation. SEM images were obtained on FEI Helios Nanolab G3 with accelerating voltage of 5.0 keV and probe current of 25 pA.

Electrochemistry Measurements

Chrono-amperometry measurements of the samples were conducted using an Ivium compactstat.h10800 potentiostat. All electrochemical experiments were performed in aqueous CO_2-saturated 0.1 M $KHCO_3$ solution (pH 6.8) using glassy carbon as counter electrode and leakless Ag/AgCl reference electrode (eDAQ) as reference electrode (scan rate 50 mV/s), unless stated otherwise. The potential was converted to RHE using the following formula

$$E(vs\ \mathrm{RHE}) = E(vs\ \mathrm{Ag/AgCl}) + 0.197\ \mathrm{V} + 0.0591 \times \mathrm{pH}$$

Raman Spectroscopy Measurements

Raman spectra acquisition was performed using a Renishaw InVia Raman microscope and 785 nm excitation laser. A Nikon N40×-NIR water-dipping objective was used for signal collection. The laser power needs to be kept below 1.5 mW to protect the sample from laser damage. The same custom-made Raman *in situ* cell (Figure S5) as in our previous publication[34] was used for the collection of Raman spectra. We would like to note that the cell is not a triphasic flow cell (which includes gas-diffusion electrodes) that are used to achieve high current in many scientific publications. The working electrode still contacts only CO_2-saturated electrolyte, and we choose a moderate flow rate (∼5 mL/min) to make the mass transfer condition comparable to an H-Cell. A grating with 1200 lines/mm was used for maximum efficiency. This limits the wavenumber coverage of each single time-resolved-SERS collection to *ca.* 250 cm^{-1}. To collect a full spectrum covering the wavenumber range between 100 and 2200 cm^{-1}, 6 scans of different wavenumber window of 3 s each are needed, resulting in a total collection of ∼18 s for each spectrum. A Raman mapping image was captured from a matrix of 7 by 7 points, with intervals of 1 μm between adjacent points. The potential was applied through an Autolab PGSTAT 101 potentiostat. All other electrochemistry setups are the same as mentioned above.

i_{rel}^{495} and i_{rel}^{LFB} Calculations

Raman spectra in the corresponding windows were fitted using sums of Gaussian peaks (see Figure S10 for some showcase examples). The relative intensities are calculated as follows

$$i_{rel}^{495} = \frac{i^{495}}{i^{495} + i^{360}}$$

https://doi.org/10.1021/jacsau.3c00129
JACS Au 2023, 3, 1890−1901

$$i_{\mathrm{rel}}^{\mathrm{LFB}} = \frac{i^{\mathrm{LFB}}}{i^{\mathrm{LFB}} + i^{\mathrm{HFB}}}$$

Product Analysis

The activity evaluation of eCO_2RR was conducted in a custom quartz H-cell. A piece of glassy carbon (~3 cm^2) served as counter electrode, and an Ag/AgCl reference electrode (eDAQ) was used for controlling the applied potential. The flow rate of CO_2 was kept at 8.7 sccm. CO, CH_4, and C_2H_4 were quantified using an Interscience online GC equipped with an FID detector. H_2 was quantified using a TCD detector and Kr as internal calibration gas. The FE was calculated using the following formula

$$\mathrm{FE}\ \% = \frac{c \cdot f \cdot F \cdot n_i}{i \cdot V_m \cdot 60\ \mathrm{sec}\ /\mathrm{min} \cdot 1{,}000{,}000\ \mathrm{ppm}} \times 100\%$$

where c is the concentration obtained from the GC (in ppm), f is the flow rate of CO_2 gas (in mL/min), F is the faradaic constant (96,485 C/mol), n_i is the number of electrons transferred to a given product (unitless), i is the average current in 1 min (A), V_m is the volume of 1 mol gas at reaction temperature and pressure (24,451 mL/mol).

■ ASSOCIATED CONTENT

Supporting Information

The Supporting Information is available free of charge at https://pubs.acs.org/doi/10.1021/jacsau.3c00129.

The Supporting Information contains experimental details on sample preparation, instrument settings and data handling procedures. Additional figures on catalyst characterization (SEM, XRD) and Raman spectra (including PCA and *k*-means clustering details) as well as a table containing a summary of Raman peak assignments in eCO_2RR on copper (PDF)

■ AUTHOR INFORMATION

Corresponding Authors

Ward van der Stam − *Inorganic Chemistry and Catalysis Group, Institute for Sustainable and Circular Chemistry and Debye Institute for Nanomaterials Science, Utrecht University, 3584 CG Utrecht, The Netherlands;* orcid.org/0000-0001-8155-5400; Email: w.vanderstam@uu.nl

Bert M. Weckhuysen − *Inorganic Chemistry and Catalysis Group, Institute for Sustainable and Circular Chemistry and Debye Institute for Nanomaterials Science, Utrecht University, 3584 CG Utrecht, The Netherlands;* orcid.org/0000-0001-5245-1426; Email: b.m.weckhuysen@uu.nl

Authors

Hongyu An − *Inorganic Chemistry and Catalysis Group, Institute for Sustainable and Circular Chemistry and Debye Institute for Nanomaterials Science, Utrecht University, 3584 CG Utrecht, The Netherlands;* orcid.org/0000-0003-4646-9819

Jim de Ruiter − *Inorganic Chemistry and Catalysis Group, Institute for Sustainable and Circular Chemistry and Debye Institute for Nanomaterials Science, Utrecht University, 3584 CG Utrecht, The Netherlands*

Longfei Wu − *Inorganic Chemistry and Catalysis Group, Institute for Sustainable and Circular Chemistry and Debye Institute for Nanomaterials Science, Utrecht University, 3584 CG Utrecht, The Netherlands;* orcid.org/0000-0001-6330-3613

Shuang Yang − *Inorganic Chemistry and Catalysis Group, Institute for Sustainable and Circular Chemistry and Debye Institute for Nanomaterials Science, Utrecht University, 3584 CG Utrecht, The Netherlands*

Florian Meirer − *Inorganic Chemistry and Catalysis Group, Institute for Sustainable and Circular Chemistry and Debye Institute for Nanomaterials Science, Utrecht University, 3584 CG Utrecht, The Netherlands;* orcid.org/0000-0001-5581-5790

Complete contact information is available at: https://pubs.acs.org/10.1021/jacsau.3c00129

Author Contributions

†H.A. and J.d.R. equally contributed to this work.

Funding

This work was supported by the Netherlands Center for Multiscale Catalytic Energy Conversion (MCEC), an NWO Gravitation program funded by the Ministry of Education, Culture and Science of the government of the Netherlands, as well as the Solar Fuels research program of the Strategic Alliance EWUU between Utrecht University, University Medical Center Utrecht, Technical University Eindhoven, and Wageningen University.

Notes

The authors declare no competing financial interest.

■ REFERENCES

(1) Wen, G.; Ren, B.; Zheng, Y.; Li, M.; Silva, C.; Song, S.; Zhang, Z.; Dou, H.; Zhao, L.; Luo, D.; Yu, A.; Chen, Z. Engineering Electrochemical Surface for Efficient Carbon Dioxide Upgrade. *Adv. Energy Mater.* **2022**, *12*, 2103289.

(2) Nitopi, S.; Bertheussen, E.; Scott, S. B.; Liu, X.; Engstfeld, A. K.; Horch, S.; Seger, B.; Stephens, I. E. L.; Chan, K.; Hahn, C.; Nørskov, J. K.; Jaramillo, T. F.; Chorkendorff, I. Progress and Perspectives of Electrochemical CO_2 Reduction on Copper in Aqueous Electrolyte. *Chem. Rev.* **2019**, *119*, 7610−7672.

(3) Overa, S.; Ko, B. H.; Zhao, Y.; Jiao, F. Electrochemical Approaches for CO_2 Conversion to Chemicals: A Journey toward Practical Applications. *Acc. Chem. Res.* **2022**, *55*, 638−648.

(4) Zheng, Y.; Vasileff, A.; Zhou, X.; Jiao, Y.; Jaroniec, M.; Qiao, S. Z. Understanding the Roadmap for Electrochemical Reduction of CO_2 to Multi-Carbon Oxygenates and Hydrocarbons on Copper-Based Catalysts. *J. Am. Chem. Soc.* **2019**, *141*, 7646−7659.

(5) Xiang, K.; Shen, F.; Fu, Y.; Wu, L.; Wang, Z.; Yi, H.; Liu, X.; Wang, P.; Liu, M.; Lin, Z.; Liu, H. Boosting CO_2 Electroreduction towards C_{2+} Products via CO* Intermediate Manipulation on Copper-Based Catalysts. *Environ. Sci.: Nano* **2022**, *9*, 911−953.

(6) Ren, D.; Gao, J.; Zakeeruddin, S. M.; Grätzel, M. New Insights into the Interface of Electrochemical Flow Cells for Carbon Dioxide Reduction to Ethylene. *J. Phys. Chem. Lett.* **2021**, *12*, 7583−7589.

(7) Xu, Y.; Li, F.; Xu, A.; Edwards, J. P.; Hung, S. F.; Gabardo, C. M.; O'Brien, C. P.; Liu, S.; Wang, X.; Li, Y.; Wicks, J.; Miao, R. K.; Liu, Y.; Li, J.; Huang, J. E.; Abed, J.; Wang, Y.; Sargent, E. H.; Sinton, D. Low Coordination Number Copper Catalysts for Electrochemical CO_2 Methanation in a Membrane Electrode Assembly. *Nat. Commun.* **2021**, *12*, 2932.

(8) Franco, F.; Rettenmaier, C.; Jeon, H. S.; Roldan Cuenya, B. Transition Metal-Based Catalysts for the Electrochemical CO_2 reduction: From Atoms and Molecules to Nanostructured Materials. *Chem. Soc. Rev.* **2020**, *49*, 6884−6946.

(9) Arán-Ais, R. M.; Gao, D.; Roldan Cuenya, B. Structure- and Electrolyte-Sensitivity in CO_2 Electroreduction. *Acc. Chem. Res.* **2018**, *51*, 2906−2917.

(10) Gao, D.; Arán-Ais, R. M.; Jeon, H. S.; Roldan Cuenya, B. Rational Catalyst and Electrolyte Design for CO_2 Electroreduction towards Multicarbon Products. *Nat. Catal.* **2019**, *2*, 198−210.
(11) García de Arquer, F. P.; Dinh, C.-T.; Ozden, A.; Wicks, J.; McCallum, C.; Kirmani, A. R.; Nam, D.-H.; Gabardo, C.; Seifitokaldani, A.; Wang, X.; Li, Y. C.; Li, F.; Edwards, J.; Richter, L. J.; Thorpe, S. J.; Sinton, D.; Sargent, E. H. CO_2 Electrolysis to Multicarbon Products at Activities Greater than 1 A cm^{-2}. *Science* **2020**, *367*, 661−666.
(12) Asperti, S.; Hendrikx, R.; Gonzalez-Garcia, Y.; Kortlever, R. Benchmarking the Electrochemical CO_2 Reduction on Polycrystalline Copper Foils: The Importance of Microstructure Versus Applied Potential. *ChemCatChem* **2022**, *14*, No. e202200540.
(13) Luo, W.; Nie, X.; Janik, M. J.; Asthagiri, A. Facet Dependence of CO_2 Reduction Paths on Cu Electrodes. *ACS Catal.* **2016**, *6*, 219−229.
(14) Gunathunge, C. M.; Li, J.; Li, X.; Hong, J. J.; Waegele, M. M. Revealing the Predominant Surface Facets of Rough Cu Electrodes under Electrochemical Conditions. *ACS Catal.* **2020**, *10*, 6908−6923.
(15) Wan, L.; Zhou, Q.; Wang, X.; Wood, T. E.; Wang, L.; Duchesne, P. N.; Guo, J.; Yan, X.; Xia, M.; Li, Y. F.; Ali, F. M.; Ulmer, U.; Jia, J.; Li, T.; Sun, W.; Ozin, G. A. Cu_2O Nanocubes with Mixed Oxidation-State Facets for (Photo)Catalytic Hydrogenation of Carbon Dioxide. *Nat. Catal.* **2019**, *2*, 889−898.
(16) Mistry, H.; Varela, A. S.; Bonifacio, C. S.; Zegkinoglou, I.; Sinev, I.; Choi, Y. W.; Kisslinger, K.; Stach, E. A.; Yang, J. C.; Strasser, P.; Cuenya, B. R. Highly Selective Plasma-Activated Copper Catalysts for Carbon Dioxide Reduction to Ethylene. *Nat. Commun.* **2016**, *7*, 12123.
(17) Zhao, Q.; Martirez, J. M. P.; Carter, E. A. Revisiting Understanding of Electrochemical CO_2 Reduction on Cu(111): Competing Proton-Coupled Electron Transfer Reaction Mechanisms Revealed by Embedded Correlated Wavefunction Theory. *J. Am. Chem. Soc.* **2021**, *143*, 6152−6164.
(18) Wu, Z. Z.; Zhang, X. L.; Niu, Z. Z.; Gao, F. Y.; Yang, P. P.; Chi, L. P.; Shi, L.; Wei, W.-s.; Liu, R.; Chen, Z.; Hu, S.; Zheng, X.; Gao, M. R. Identification of Cu(100)/Cu(111) Interfaces as Superior Active Sites for CO Dimerization during CO_2 Electroreduction. *J. Am. Chem. Soc.* **2022**, *144*, 259−269.
(19) Rossi, K.; Buonsanti, R. Shaping Copper Nanocatalysts to Steer Selectivity in the Electrochemical CO_2 Reduction Reaction. *Acc. Chem. Res.* **2022**, *55*, 629−637.
(20) Zaza, L.; Rossi, K.; Buonsanti, R. Well-Defined Copper-Based Nanocatalysts for Selective Electrochemical Reduction of CO_2 to C_2 Products. *ACS Energy Lett.* **2022**, *7*, 1284−1291.
(21) de Gregorio, G. L.; Burdyny, T.; Loiudice, A.; Iyengar, P.; Smith, W. A.; Buonsanti, R. Facet-Dependent Selectivity of Cu Catalysts in Electrochemical CO_2 Reduction at Commercially Viable Current Densities. *ACS Catal.* **2020**, *10*, 4854−4862.
(22) Sebastián-Pascual, P.; Mezzavilla, S.; Stephens, I. E. L.; Escudero-Escribano, M. Structure-Sensitivity and Electrolyte Effects in CO_2 Electroreduction: From Model Studies to Applications. *ChemCatChem* **2019**, *11*, 3626−3645.
(23) Banerjee, S.; Gerke, C. S.; Thoi, V. S. Guiding CO_2RR Selectivity by Compositional Tuning in the Electrochemical Double Layer. *Acc. Chem. Res.* **2022**, *55*, 504−515.
(24) Li, Z.; Yang, Y.; Yin, Z.; Wei, X.; Peng, H.; Lyu, K.; Wei, F.; Xiao, L.; Wang, G.; Abruña, H. D.; Lu, J.; Zhuang, L. Interface-Enhanced Catalytic Selectivity on the C_2 Products of CO_2 Electroreduction. *ACS Catal.* **2021**, *11*, 2473−2482.
(25) Zhu, S.; Delmo, E. P.; Li, T.; Qin, X.; Tian, J.; Zhang, L.; Shao, M. Recent Advances in Catalyst Structure and Composition Engineering Strategies for Regulating CO_2 Electrochemical Reduction. *Adv. Mater.* **2021**, *33*, 2005484.
(26) Zhan, C.; Dattila, F.; Rettenmaier, C.; Bergmann, A.; Kühl, S.; García-Muelas, R.; López, N.; Cuenya, B. R. Revealing the CO Coverage-Driven C−C Coupling Mechanism for Electrochemical CO_2 Reduction on Cu_2O Nanocubes via Operando Raman Spectroscopy. *ACS Catal.* **2021**, *11*, 7694−7701.
(27) Wang, J.; Tan, H. Y.; Zhu, Y.; Chu, H.; Chen, H. M. Linking the Dynamic Chemical State of Catalysts with the Product Profile of Electrocatalytic CO_2 Reduction. *Angew. Chem., Int. Ed.* **2021**, *60*, 17254−17267.
(28) Lai, W.; Ma, Z.; Zhang, J.; Yuan, Y.; Qiao, Y.; Huang, H. Dynamic Evolution of Active Sites in Electrocatalytic CO_2 Reduction Reaction: Fundamental Understanding and Recent Progress. *Adv. Funct. Mater.* **2022**, *32*, 2111193.
(29) Jiang, Y.; Wang, X.; Duan, D.; He, C.; Ma, J.; Zhang, W.; Liu, H.; Long, R.; Li, Z.; Kong, T.; Loh, X. J.; Song, L.; Ye, E.; Xiong, Y. Structural Reconstruction of Cu_2O Superparticles toward Electrocatalytic CO_2 Reduction with High C_{2+} Products Selectivity. *Adv. Sci.* **2022**, *9*, 2105292.
(30) Didomenico, R. C.; Hanrath, T. Pulse Symmetry Impacts the C_2 Product Selectivity in Pulsed Electrochemical CO_2 Reduction. *ACS Energy Lett.* **2022**, *7*, 292−299.
(31) Zou, Y.; Wang, S. An Investigation of Active Sites for Electrochemical CO_2 Reduction Reactions: From In Situ Characterization to Rational Design. *Adv. Sci.* **2021**, *8*, 2003579.
(32) Simon, G. H.; Kley, C. S.; Roldan Cuenya, B. Potential-Dependent Morphology of Copper Catalysts During CO_2 Electroreduction Revealed by In Situ Atomic Force Microscopy. *Angew. Chem., Int. Ed.* **2021**, *60*, 2561−2568.
(33) Gunathunge, C. M.; Li, X.; Li, J.; Hicks, R. P.; Ovalle, V. J.; Waegele, M. M. Spectroscopic Observation of Reversible Surface Reconstruction of Copper Electrodes under CO_2 Reduction. *J. Phys. Chem. C* **2017**, *121*, 12337−12344.
(34) An, H.; Wu, L.; Mandemaker, L. D. B.; Yang, S.; de Ruiter, J.; Wijten, J. H. J.; Janssens, J. C. L.; Hartman, T.; van der Stam, W.; Weckhuysen, B. M. Sub-Second Time-Resolved Surface-Enhanced Raman Spectroscopy Reveals Dynamic CO Intermediates during Electrochemical CO_2 Reduction on Copper. *Angew. Chem., Int. Ed.* **2021**, *60*, 16576−16584.
(35) de Ruiter, J.; An, H.; Wu, L.; Gijsberg, Z.; Yang, S.; Hartman, T.; Weckhuysen, B. M.; van der Stam, W. Probing the Dynamics of Low-Overpotential CO_2-to-CO Activation on Copper Electrodes with Time-Resolved Raman Spectroscopy. *J. Am. Chem. Soc.* **2022**, *144*, 15047−15058.
(36) Gunathunge, C. M.; Ovalle, V. J.; Li, Y.; Janik, M. J.; Waegele, M. M. Existence of an Electrochemically Inert CO Population on Cu Electrodes in Alkaline pH. *ACS Catal.* **2018**, *8*, 7507−7516.
(37) Moradzaman, M.; Mul, G. In Situ Raman Study of Potential-Dependent Surface Adsorbed Carbonate, CO, OH, and C Species on Cu Electrodes During Electrochemical Reduction of CO_2. *ChemElectroChem* **2021**, *8*, 1478−1485.
(38) Li, H.; Wei, P.; Gao, D.; Wang, G. In Situ Raman Spectroscopy Studies for Electrochemical CO_2 Reduction over Cu Catalysts. *Curr. Opin. Green Sustainable Chem.* **2022**, *34*, 100589.
(39) Steimecke, M.; Araújo-Cordero, A. M.; Dieterich, E.; Bron, M. Probing Individual Cuprous Oxide Microcrystals towards Carbon Dioxide Reduction by Using In Situ Raman-Coupled Scanning Electrochemical Microscopy. *ChemElectroChem* **2022**, *9*, No. e202101221.
(40) Guo, S. X.; Bentley, C. L.; Kang, M.; Bond, A. M.; Unwin, P. R.; Zhang, J. Advanced Spatiotemporal Voltammetric Techniques for Kinetic Analysis and Active Site Determination in the Electrochemical Reduction of CO_2. *Acc. Chem. Res.* **2022**, *55*, 241−251.
(41) Sebastián-Pascual, P.; Escudero-Escribano, M. Addressing the Interfacial Properties for CO Electroreduction on Cu with Cyclic Voltammetry. *ACS Energy Lett.* **2020**, *5*, 130−135.
(42) Dutta, A.; Rahaman, M.; Hecker, B.; Drnec, J.; Kiran, K.; Zelocualtecatl Montiel, I.; Jochen Weber, D.; Zanetti, A.; Cedeño López, A.; Martens, I.; Broekmann, P.; Oezaslan, M. CO_2 Electrolysis − Complementary Operando XRD, XAS and Raman Spectroscopy Study on the Stability of CuxO Foam Catalysts. *J. Catal.* **2020**, *389*, 592−603.
(43) Chen, C.; Yan, X.; Wu, Y.; Liu, S.; Sun, X.; Zhu, Q.; Feng, R.; Wu, T.; Qian, Q.; Liu, H.; Zheng, L.; Zhang, J.; Han, B. The In situ Study of Surface Species and Structures of Oxide-Derived Copper

https://doi.org/10.1021/jacsau.3c00129
JACS Au 2023, 3, 1890−1901

Catalysts for Electrochemical CO_2 reduction. *Chem. Sci.* **2021**, *12*, 5938−5943.
(44) Dattila, F.; Garcıa-Muelas, R.; López, N. Active and Selective Ensembles in Oxide-Derived Copper Catalysts for CO_2 Reduction. *ACS Energy Lett.* **2020**, *5*, 3176−3184.
(45) Yuan, X.; Chen, S.; Cheng, D.; Li, L.; Zhu, W.; Zhong, D.; Zhao, Z. J.; Li, J.; Wang, T.; Gong, J. Controllable Cu^0-Cu^+ Sites for Electrocatalytic Reduction of Carbon Dioxide. *Angew. Chem., Int. Ed.* **2021**, *60*, 15344−15347.
(46) Liu, W.; Zhai, P.; Li, A.; Wei, B.; Si, K.; Wei, Y.; Wang, X.; Zhu, G.; Chen, Q.; Gu, X.; Zhang, R.; Zhou, W.; Gong, Y. Electrochemical CO_2 Reduction to Ethylene by Ultrathin CuO Nanoplate Arrays. *Nat. Commun.* **2022**, *13*, 1877.
(47) Chernyshova, I. V.; Somasundaran, P.; Ponnurangam, S. On the Origin of the Elusive First Intermediate of CO_2 Electroreduction. *Proc. Natl. Acad. Sci. U.S.A.* **2018**, *115*, E9261−E9270.
(48) Jiang, S.; Klingan, K.; Pasquini, C.; Dau, H. New Aspects of Operando Raman Spectroscopy Applied to Electrochemical CO_2 Reduction on Cu Foams. *J. Chem. Phys.* **2019**, *150*, 041718.
(49) Klingan, K.; Kottakkat, T.; Jovanov, Z. P.; Jiang, S.; Pasquini, C.; Scholten, F.; Kubella, P.; Bergmann, A.; Roldan Cuenya, B.; Roth, C.; Dau, H. Reactivity Determinants in Electrodeposited Cu Foams for Electrochemical CO_2 Reduction. *ChemSusChem* **2018**, *11*, 3449−3459.
(50) Shan, W.; Liu, R.; Zhao, H.; He, Z.; Lai, Y.; Li, S.; He, G.; Liu, J. In Situ Surface-Enhanced Raman Spectroscopic Evidence on the Origin of Selectivity in CO_2 Electrocatalytic Reduction. *ACS Nano* **2020**, *14*, 11363−11372.
(51) Zhao, Y.; Chang, X.; Malkani, A. S.; Yang, X.; Thompson, L.; Jiao, F.; Xu, B. Speciation of Cu Surfaces during the Electrochemical CO Reduction Reaction. *J. Am. Chem. Soc.* **2020**, *142*, 9735−9743.
(52) Li, J.; Chang, X.; Zhang, H.; Malkani, A. S.; Cheng, M. J.; Xu, B.; Lu, Q. Electrokinetic and in Situ Spectroscopic Investigations of CO Electrochemical Reduction on Copper. *Nat. Commun.* **2021**, *12*, 3264.
(53) Yang, K.; Kas, R.; Smith, W. A. In Situ Infrared Spectroscopy Reveals Persistent Alkalinity near Electrode Surfaces during CO_2 Electroreduction. *J. Am. Chem. Soc.* **2019**, *141*, 15891−15900.
(54) Burdyny, T.; Smith, W. A. CO_2 Reduction on Gas-Diffusion Electrodes and Why Catalytic Performance Must Be Assessed at Commercially-Relevant Conditions. *Energy Environ. Sci.* **2019**, *12*, 1442−1453.
(55) Gauthier, J. A.; Stenlid, J. H.; Abild-Pedersen, F.; Head-Gordon, M.; Bell, A. T. The Role of Roughening to Enhance Selectivity to C_{2+} Products during CO_2 Electroreduction on Copper. *ACS Energy Lett.* **2021**, *6*, 3252−3260.
(56) Asiri, A. M.; Gao, J.; Khan, S. B.; Alamry, K. A.; Marwani, H. M.; Khan, M. S. J.; Adeosun, W. A.; Zakeeruddin, S. M.; Ren, D.; Grätzel, M. Revisiting the Impact of Morphology and Oxidation State of Cu on CO_2 Reduction Using Electrochemical Flow Cell. *J. Phys. Chem. Lett.* **2022**, *13*, 345−351.
(57) Goodpaster, J. D.; Bell, A. T.; Head-Gordon, M. Identification of Possible Pathways for C-C Bond Formation during Electrochemical Reduction of CO_2: New Theoretical Insights from an Improved Electrochemical Model. *J. Phys. Chem. Lett.* **2016**, *7*, 1471−1477.
(58) Garza, A. J.; Bell, A. T.; Head-Gordon, M. Mechanism of CO_2 Reduction at Copper Surfaces: Pathways to C_2 Products. *ACS Catal.* **2018**, *8*, 1490−1499.
(59) Liu, X.; Xiao, J.; Peng, H.; Hong, X.; Chan, K.; Nørskov, J. K. Understanding Trends in Electrochemical Carbon Dioxide Reduction Rates. *Nat. Commun.* **2017**, *8*, 15438.
(60) Salimon, J.; Hernández-Romero, R. M.; Kalaji, M. The Dynamics of the Conversion of Linear to Bridge Bonded CO on Cu. *J. Electroanal. Chem.* **2002**, *538*−*539*, 99−108.
(61) Chou, T. C.; Chang, C. C.; Yu, H. L.; Yu, W. Y.; Dong, C. L.; Velasco-Vélez, J. J.; Chuang, C. H.; Chen, L. C.; Lee, J. F.; Chen, J. M.; Wu, H. L. Controlling the Oxidation State of the Cu Electrode and Reaction Intermediates for Electrochemical CO_2 Reduction to Ethylene. *J. Am. Chem. Soc.* **2020**, *142*, 2857−2867.
(62) Gu, Z.; Shen, H.; Chen, Z.; Yang, Y.; Yang, C.; Ji, Y.; Wang, Y.; Zhu, C.; Liu, J.; Li, J.; Sham, T. K.; Xu, X.; Zheng, G. Efficient Electrocatalytic CO_2 Reduction to C_{2+} Alcohols at Defect-Site-Rich Cu Surface. *Joule* **2021**, *5*, 429−440.

NOTE ADDED AFTER ASAP PUBLICATION

This paper was published ASAP on July 6, 2023, with an error in Figure 1. The corrected version was reposted with the issue on July 24, 2023.

https://doi.org/10.1021/jacsau.3c00129
JACS Au 2023, 3, 1890−1901